

Geochemistry, Geophysics, Geosystems

-

RESEARCH ARTICLE

10.1029/2023GC011336

Key Points:

- Magnetic methods document titanomagnetite nanolites in rhyolitic materials from Glass Mountain, Medicine Lake Volcano, California
- Titanomagnetite number densities for pumice, obsidian, and vesicular obsidian span 10¹² to 10²⁰ m⁻³ of solid material
- Titanomagnetite crystals already existed in extremely high numberabundance at the time of magma ascent and bubble nucleation

Supporting Information:

Supporting Information may be found in the online version of this article.

Correspondence to:

S. Brachfeld, brachfelds@montclair.edu

Citation:

Brachfeld, S., McCartney, K. N., Hammer, J. E., Shea, T., & Giachetti, T. (2024). Evaluating the role of titanomagnetite in bubble nucleation: Rock magnetic detection and characterization of nanolites and ultra-nanolites in rhyolite pumice and obsidian from Glass Mountain, California. *Geochemistry, Geophysics, Geosystems*, 25, e2023GC011336. https://doi.org/10.1029/2023GC011336

Received 7 NOV 2023 Accepted 17 FEB 2024

Author Contributions:

Conceptualization: Stefanie Brachfeld, Kelly N. McCartney, Julia E. Hammer, Thomas Shea, Thomas Giachetti Formal analysis: Stefanie Brachfeld, Julia E. Hammer, Thomas Shea, Thomas Giachetti Funding acquisition: Stefanie Brachfeld, Julia E. Hammer, Thomas Shea Investigation: Stefanie Brachfeld, Julia E. Hammer, Thomas Shea, Thomas Giachetti

© 2024 The Authors. Geochemistry, Geophysics, Geosystems published by Wiley Periodicals LLC on behalf of American Geophysical Union.
This is an open access article under the terms of the Creative Commons Attribution License, which permits use, distribution and reproduction in any medium, provided the original work is properly cited.

Evaluating the Role of Titanomagnetite in Bubble Nucleation: Rock Magnetic Detection and Characterization of Nanolites and Ultra-Nanolites in Rhyolite Pumice and Obsidian From Glass Mountain, California

Stefanie Brachfeld¹, Kelly N. McCartney², Julia E. Hammer², Thomas Shea², and Thomas Giachetti³

¹Montclair State University, Montclair, NJ, USA, ²University of Hawai'i at Mānoa, Honolulu, HI, USA, ³University of Oregon, Eugene, OR, USA

Abstract We document the presence, composition, and number density (TND) of titanomagnetite nanolites and ultra-nanolites in aphyric rhyolitic pumice, obsidian, and vesicular obsidian from the 1060 CE Glass Mountain volcanic eruption of Medicine Lake Volcano, California, using magnetic methods, Curie temperatures indicate compositions of Fe_{2.40}Ti_{0.60}O₄ to Fe₃O₄. Rock-magnetic parameters sensitive to domain state, which is dependent on grain volume, indicate a range of particle sizes spanning superparamagnetic (<50-80 nm) to multidomain (>10 µm) particles. Cylindrical cores drilled from the centers of individual pumice clasts display anisotropy of magnetic susceptibility with prolate fabrics, with the highest degree of anisotropy coinciding with the highest vesicularity. Fabrics within a pumice clast require particle alignment within a fluid, and are interpreted to result from the upward transport of magma driven by vesiculation, ensuing bubble growth, and shearing in the conduit. Titanomagnetite number density (TND) is calculated from titanomagnetite volume fraction, which is determined from ferromagnetic susceptibility. TND estimates for monospecific assemblages of 1,000 nm-10 nm cubes predict 10^{12} to 10^{20} m⁻³ of solid material, respectively. TND estimates derived using a power law distribution of grain sizes predict 10¹⁸ to 10¹⁹ m⁻³. These ranges agree well with TND determinations of 10¹⁸ to 10²⁰ m⁻³ made by McCartney et al. (2024), and are several orders of magnitude larger than the number density of bubbles in these materials. These observations are consistent with the hypothesis that titanomagnetite crystals already existed in extremely high number-abundance at the time of magma ascent and bubble nucleation.

Plain Language Summary We use magnetism experiments to prove that nanometer-sized magnetic particles are present in volcanic rocks with low iron content and few visible crystals. Nanolites (particles between 30 and 1,000 nm) and ultra-nanolites (particles smaller than 30 nm) are extremely difficult to detect in volcanic rocks composed mainly of glass using conventional methods such as optical and electron microscopy. Titanomagnetite nano-particles may play a role in controlling the explosiveness of volcanic eruptions. The magnetic signatures of minerals can be used to determine their chemical composition, particle size range, and particle abundance. Pumice and obsidian contain the mineral titanomagnetite, with no evidence of prolonged crystallization at high oxygen levels at the Earth's surface. Observed magnetic behaviors are very similar to those of previously published studies of titanomagnetite in the 10–1,000 nm size range, and similar to mathematical models that simulate this size range. We find that pumice clasts have a magnetic fabric, suggesting that the nanolites and ultra-nanolites were aligned in spatial patterns before the magma solidified, with stronger alignment coinciding with high degrees of vesicularity. Our results indicate that titanomagnetite crystals are highly abundant, and had crystallized in the magma chamber before the eruption.

1. Introduction

Nanolites, crystalline particles with diameters <1,000 nm, have been described in a variety of volcanic rocks and proposed as drivers of increased eruption explosivity through increasing magma viscosity and impeding the release of volatiles, and by facilitating bubble nucleation (Aubin et al., 2023; Cáceres et al., 2020, 2021; Di Genova et al., 2017; Gardner & Denis, 2004; Giachetti et al., 2010, 2011; Hajimirza et al., 2021; Knafelc et al., 2022; Mujin et al., 2017; Mujin & Nakamura, 2014; Pistone et al., 2022; Sharp et al., 1996; Shea, 2017; Vigliotti et al., 2022; Yoshida et al., 2023), motivating interest in quantifying the composition and number density

BRACHFELD ET AL. 1 of 15

and-conditions) on Wiley Online Library for rules of use; OA articles are governed by the applicable Creative Commons Licens

Methodology: Stefanie Brachfeld, Kelly N. McCartney, Julia E. Hammer, Thomas Shea, Thomas Giachetti Project administration:

Stefanie Brachfeld, Julia E. Hammer Supervision: Stefanie Brachfeld, Julia E. Hammer

Validation: Stefanie Brachfeld, Julia

E. Hammer, Thomas Shea, Thomas Giachetti

Visualization: Stefanie Brachfeld, Julia

E. Hammer, Thomas Shea
Writing – original draft:

Stefanie Brachfeld, Kelly N. McCartney, Julia E. Hammer, Thomas Shea,

Thomas Giachetti
Writing – review & editing:

Stefanie Brachfeld, Kelly N. McCartney, Julia E. Hammer, Thomas Shea, Thomas Giachetti of nanolites in eruptive and effusive volcanic rocks. Petrographic detection and compositional analysis of coarse nanolites and microlites is possible via transmission electron microscopy (TEM), scanning electron microscopy (SEM), and Raman spectroscopy, particularly when particles are abundant (>0.5 vol.%). Petrographic detection and compositional analyses are extremely challenging for ultra-nanolites, defined as particles <30 nm (Mujin & Nakamura, 2014), and generally not productive in aphyric volcanic rocks unless a substantial number of TEM fields of view are examined. Consequently, while microlite abundances in volcanic rocks have been reported (e.g., Giachetti et al., 2010, 2011), quantifying nanolite and ultra-nanolite abundance remains elusive.

Titanomagnetite ($Fe_{3-1}Ti_{1}O_{4}$) is a crystal phase likely to enhance bubble nucleation in magma (Aubin et al., 2023; Cáceres et al., 2021; Di Genova et al., 2020; Gardner & Denis, 2004; Giachetti et al., 2010, 2011; McCartney et al., 2024; Shea, 2017). Even at very low abundances (<0.01 vol.%), the distinctive magnetic signatures of titanomagnetite can be used to confirm its presence and constrain its mineralogy, domain state, and abundance. Titanomagnetite is a ferrimagnetic mineral that carries a spontaneous magnetization in the absence of an applied magnetic field. Ferrimagnetic minerals display a progression of magnetic behavior as a function of domain state, which in turn is a function of mineralogy and grain volume. Superparamagnetic (Superparamagnetic particles (SP)) behavior is exhibited by magnetite (Fe₃O₄) and titanomagnetite particles <20–50 nm and $<\sim80$ nm, respectively (Dunlop & Özdemir, 1997). SP particles display high values of susceptibility (χ) at room temperature, a measurement made in the presence of a weak applied field, but cannot carry a stable remanence at or above room temperature. Stable-single-domain (stable single domain (SSD)) particles (~50-1,000 nm for titanomagnetite) carry strong natural and induced remanent magnetizations such as thermoremanent magnetization (TRM) and anhysteretic remanent magnetization (ARM) at temperatures below their blocking temperatures, and are stable over geologic time. SSD grains exhibit high values of coercivity (H_C) and lower values of χ (Argyle & Dunlop, 1990; Dunlop, 1986, 2002a, 2002b; Dunlop & Argyle, 1997; Dunlop & Özdemir, 1997; Maher, 1988; Özdemir & Banerjee, 1982). Titanomagnetite in the 1-10 µm size range, historically referred to as transitional "pseudo-single-domain" (PSD) particles, display single vortex and multi-vortex behavior (Dunlop 2002a, 2002b; Egli, 2021; Roberts et al., 2017; Tauxe et al., 2002; Williams & Dunlop, 1995), and display multidomain (MD) behavior in particles larger than 10 μm (Day et al., 1977; Dunlop & Özdemir, 1997), with amplitudes of TRM, ARM, and H_C gradually decreasing as particle size coarsens above 1 µm and χ increasing slightly between 1 and 100 μm for moderate- to high-Ti titanomagnetite (Day et al., 1977; Hartstra, 1982; Parry, 1965).

Mapping a single value of TRM, ARM, H_C , χ , or any other magnetic parameter to a specific particle size is not possible due to the multiple controls on magnetic behavior, including grain volume, mineralogy, particle shape, degree of oxidation, degree of cation substitution, and presence of defects and dislocations, all of which impact energy barriers to magnetization changes (which is the basis for measuring magnetic parameters), and degree of particle interactions, which can create constructive or destructive interactions that impact the amplitudes of these parameters (e.g., Sugiura, 1979). However, combinations of rock magnetic observations can confirm the presence of ferrimagnetic minerals and constrain their abundance, range of compositions, and range of domain-states present in a mixture (such as rocks, sediment, and soil), allowing us to estimate plausible titanomagnetite number densities. In a pair of companion papers, we use rock magnetic methods to document the presence of nanolites and ultra-nanolites in aphyric rhyolitic pumice, obsidian, and vesicular obsidian from the 1060 CE Glass Mountain eruption of Medicine Lake Volcano (California) and calculate estimates of their number density (this study). In the companion paper, McCartney et al., 2024 present a low-temperature method for titanomagnetite number density (TND) calculations that targets ultra-nanolites and compares ultra-nanolite abundance with pumice physical properties to evaluate hypotheses concerning the timing of titanomagnetite crystallization and evaluate the role of titanomagnetite crystalls in bubble nucleation.

2. Materials

This study examines pumice, obsidian, and vesicular obsidian from the 1060 CE Glass Mountain eruption of the Medicine Lake Volcano, CA, USA (Figure 1). McCartney et al. (2024), provide a synthesis of the body of knowledge concerning magma chemical composition, volatile content, eruptive style, volume of eruptive products, as well as the petrography, textural and physical properties, and bubble number densities of the eruptive products. In brief, the 1060 CE eruption produced rhyolitic pumice fall deposits, followed by rhyolitic and dacitic obsidian flows and a series of domes (Grove et al., 1997; Heiken, 1978). Pumice clasts studied here are rhyolitic (\sim 70–75% SiO₂) and have been described in the literature as colorless glass that is crystal-poor to crystal-free, with the exception of trace amounts of plagioclase and orthopyroxene microlites (Heiken, 1978).

BRACHFELD ET AL. 2 of 15

Figure 1. (a) Location of Glass Mountain in northern California, western United States (image generated using GeoMapApp, http://www.geomapapp.org). (b) Google Earth image showing the 1060 CE Glass Mountain obsidian flow (gray and dark gray areas) and pumice quarry (light gray area marked by the dashed white ellipse). Red circles show the obsidian sample collection areas. (Google Earth v. 10.43.0.2 (7 October 2017-newer data), Glass Mountain, California). 41° 36.03″N, 121° 30.17″W. Eye alt. 17 km, Landsat/Copernicus, https://earth.google.com/web/ [3 January 2024].

Rock magnetic analyses were carried out on pumice clasts from subunits of the main fall deposit (designated here as A2, $B_{\rm max}$, C, F, and M), cylindrical cores drilled from pumice clast interiors, obsidian pieces from two flow lobes designated as the northern and southern obsidian flows, and a vesicular obsidian flow adjacent to the southern obsidian flow lobe (Figure 1). Pumice clasts analyzed range in mass from \sim 1 to 11 g, are generally white or gray and crystal-poor to crystal-free glass (Giachetti et al., 2021; McCartney et al., 2024; Trafton & Giachetti, 2021). We avoided clasts with visible surface staining or pink/brown color changes that could indicate weathering rinds and/or formation of secondary oxides after the eruption during cooling at the Earth's surface (e.g., Knafelc et al., 2022). Vesicularities and densities of individual clasts are reported in McCartney et al. (2024). Obsidian samples from the Northern flow consist of 3-mm diameter and \sim 5-10-mm-long cores drilled from a single block of obsidian chosen for the absence of microlites. Samples from the southern obsidian flow and the southern vesicular obsidian flow consist of \sim 1-cm pieces.

3. Methods

3.1. Room Temperature Magnetic Measurements

Room temperature rock magnetic analyses were conducted at Montclair State University to characterize the magnetic mineral domain state, composition, and abundance. Low-field mass-normalized magnetic susceptibility (χ_{LF}) was measured on an AGICO MFK2-FA Kappabridge in an applied field of 200 A/m and a frequency of 976 Hz. χ_{LF} amplitude is a function of ferrimagnetic mineral abundance relative to paramagnetic and diamagnetic material abundance. Mass-normalized χ_{LF} was converted to volume-normalized k using individual specimen bulk densities for pumice clasts and southern vesicular flow pieces (see McCartney et al., 2024) and a density of 2,430 kg/m³ for obsidian (Giachetti et al., 2015).

A modified frequency dependence of susceptibility parameter (% $\chi_{\rm fd}$) was determined by making a second χ measurement at 3,904 Hz and calculating:

$$\%\chi'_{\rm fd} = 100 * \frac{\left(\chi_{976 \text{ Hz}} - \chi_{3,904 \text{ Hz}}\right)}{\chi_{976 \text{ Hz}}}.$$
 (1)

This parameter is described as "modified" because $\%\chi_{\rm fd}$ is historically calculated from χ measurements at frequencies of 470 and 4,700 Hz, the two frequencies available on the Bartington MS2B sensor. Our $\%\chi_{\rm fd}$ values are interpreted as minima for this parameter due to the narrower frequency range. $\%\chi_{\rm fd}$ is a rapid detection tool for SP content, where values of several % or higher are interpreted to reflect the presence of SP particles (Dearing

BRACHFELD ET AL. 3 of 15

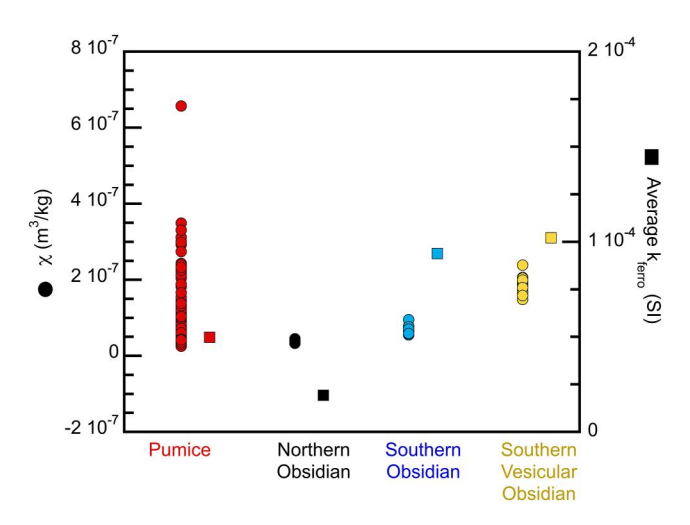


Figure 2. Mass-normalized low-field magnetic susceptibility (χ_{LF}) for Glass Mountain eruptive and effusive products (circles), with values given on the left-hand vertical axis, and the average volume-normalized ferromagnetic susceptibility (k_{ferro} , squares) plotted on the right-hand vertical axis (see Table 1). Although the number of specimens for each sample set varies, the eruptive products generally have overlapping ranges of values. Average k_{ferro} values are used to calculate the volume fraction of titanomagnetite (Table 1).

et al., 1996). We report $\%\chi_{\rm fd}' = 0$ for samples where Equation 1 yields negative values (Table S1, Brachfeld et al., 2024).

Anhysteretic Remanent Magnetization (ARM) acquisition allows detection of ferrimagnetic particles in the SSD or larger domain state. ARM was measured on cylindrically cored pumice, obsidian cores and pieces, and vesicular obsidian pieces on an AGICO JR-6 Spinner Magnetometer. These samples were used for ARM because they could be oriented in the sample holder. ARM was imparted on a D-tech 2,000 Alternating Field and ARM unit in a peak alternating field of 100 mT and direct current (DC) bias fields ($H_{\rm DC}$) of 0.05–0.20 mT. ARM intensity was converted to susceptibility of ARM ($\chi_{\rm ARM}$) by dividing the mass-normalized ARM value by the intensity of $H_{\rm DC}$ in units of A/m.

Hysteresis loops and first order reversal curves (FORCs) were measured on a Princeton Measurements Corp. Vibrating Sample Magnetometer. Hysteresis loops were mass normalized and the high-field slope of the M-H curve (χ_{HF}) was calculated using the induced magnetization values between 0.7 and 1 T. χ_{HF} was used to remove the diamagnetic and paramagnetic contributions from both the induced magnetization and low field susceptibility. Saturation magnetization (M_S), saturation remanence (M_R), and bulk coercivity (H_C) were determined from the diamagnetic/paramagnetic corrected hysteresis loops. The coercivity of remanence (H_{CR}) was determined from the DC demagnetization of an initial 1-T isothermal remanent magnetization. FORC data were processed with FORCinel software version 3.08 using the VARIFORC smoothing protocol (Egli, 2013; Harrison & Feinberg, 2008; Harrison et al., 2018).

3.2. High-Temperature Magnetic Measurements

Thermomagnetic curves were measured on an AGICO MFK2-FA Kappabridge in a flowing argon gas atmosphere. Approximately 500 mg of sample was powdered and susceptibility was measured continuously during heating and cooling between 20 and 700°C in order to detect temperature-dependent order-disorder transitions. The Curie temperature ($T_{\rm C}$), the transition from ferrimagnetic ordering below $T_{\rm C}$ to paramagnetic behavior above $T_{\rm C}$, manifests as an abrupt drop in the amplitude of susceptibility across the transition temperatures of the minerals present in the sample. Naturally occurring titanomagnetite typically displays compositions of $Fe_{2.4}Ti_{0.60}O_4$ to Fe_3O_4 , with Curie temperatures of ~150–200°C through 580°C, respectively (Lattard et al., 2006). The transition temperature and width of the transition is affected by the range of compositions present in the sample, degree of oxidation, magnetic particle size distribution, and degree of cation substitution for Fe. We use Curie temperature

BRACHFELD ET AL. 4 of 15

525 2027, 2024, 4, Downloaded from https://agupubs.onlinelibrary.wiley.com/doi/10.1029/2023GC011336, Wiley Online Library on [24/04/2024]. See the Terms and Conditions (https://onlinelibrary.wiley.com/terms-ad-conditions) on Wiley Online Library for rules of use; OA articles are governed by

determinations to infer the magnetic mineralogy using the compilation of Lattard et al., 2006 and the polynomial expression for $T_{\rm C}$ of Bleil and Petersen (1982).

3.3. Titanomagnetite Volume Fraction

Average titanomagnetite volume fraction for pumice and obsidian is determined in two ways: (a) by dividing the sample set's average volume-normalized ferromagnetic susceptibility ($k_{\rm ferro}$) by the volume-normalized susceptibility of the carrier mineral ($k_{\rm carrier}$), and (b) by dividing the sample set's average volume-normalized saturation magnetization ($M_{\rm S}$, corrected for the paramagnetic and diamagnetic contributions) by the volume-normalized $M_{\rm S}$ of the carrier mineral ($M_{\rm S-carrier}$). The paramagnetic contribution to bulk susceptibility ranges from ~7% to 94% in these rhyolitic materials (Table S1). Therefore, using $k_{\rm ferro}$ and paramagnetic-corrected $M_{\rm S}$ to calculate the volume fraction prevents the inflation of TND values.

Our low-field susceptibility (χ_{LF}) and M_S measurements were mass-normalized because the majority of samples are irregularly shaped clasts (Figure 2, Table S1). We use the following steps to convert mass-normalized χ_{LF} values to volume-normalized k_{ferro} values:

$$\chi_{\text{ferro}} = \chi_{\text{LF}} - \chi_{\text{HF}} \tag{2}$$

where $\chi_{\rm ferro}$ is the mass-normalized ferromagnetic susceptibility, $\chi_{\rm LF}$ is the low-field mass-normalized susceptibility measured at 976 Hz, and $\chi_{\rm HF}$ is the high-field magnetic susceptibility calculated from the slope of the hysteresis loop between 0.7 and 1 T (Table S1). $\chi_{\rm ferro}$ in m³/kg is then converted to volume-normalized $k_{\rm ferro}$ (dimensionless SI) according to:

$$k_{\text{ferro}} = \chi_{\text{ferro}} \times \rho_{\text{sample}}$$
 (3)

where ρ_{sample} is the measured bulk density for individual pumice and vesicular obsidian samples, and the dense rock equivalent (DRE) of 2,430 kg/m³ for the northern and southern obsidian flow samples (McCartney et al., 2024). Similarly, M_{S} is converted to volume-normalized units (A/m) by multiplying M_{S} in Am²/kg by sample density in m³/kg.

The average volume fraction of titanomagnetite for each sample type is calculated as

volume fraction =
$$\frac{\text{Average } k_{\text{ferro}}}{k_{\text{carrier mineral}}}$$
 (4)

and

volume fraction =
$$\frac{\text{Average } M_S}{M_{S-carrier mineral}}$$
 (5)

where the carrier mineral composition is determined from the Curie temperature.

3.4. Anisotropy of Magnetic Susceptibility

Seven cylindrical pumice cores were analyzed for anisotropy of magnetic susceptibility (AMS) on an AGICO KLY4 Kappabridge, the instrument available at the beginning of this project. Pumice cores were trimmed after susceptibility measurements to fit the JR6 spinner magnetometer sample holder for ARM analyses. These trimmed samples were not remeasured on the new MFK2-FA instrument, which was acquired during this project, as their lengths had changed, and some cores fractured during trimming or had already been subjected to high-field treatments. AMS is a petrofabric technique that characterizes the orientation of paramagnetic and ferrimagnetic minerals in geologic samples in order to relate the alignment of magnetic particles to an environmental process, for example, flow direction in lava flows or pyroclastic density currents, and locating ancient volcanic vents (Ellwood, 1982; Ort et al., 2015; Palmer et al., 1996; Wolff et al., 1989). Pumice clasts are comprised of volcanic glass, which is magnetically isotropic. Therefore, fabrics in pumice clasts may indicate spatial arrangements of magnetic particles within the glass. In addition, clasts formed from air fall deposits are unoriented,

BRACHFELD ET AL. 5 of 15

15252027, 2024, 4, Downloaded from https://agupubs.onlinelibrary.wiley.com/doi/10.1029/2023GC011356, Wiley Online Library on [24/04/2024]. See the Terms and Conditions (https://onlinelibrary.wiley.com/terms-and-conditions) on Wiley Online Library for rules of use; OA articles are governed by the applicable Creative Commons Licenses

 Table 1

 Titanomagnetite Volume Fraction and Number Density

Sample set	Average k_{ferro} (SI)	a Min vol fraction from k_{ferro}	a Max vol fraction from k_{ferro}	Average $M_{\rm S}$ (A/m)	b Min vol fraction from M_{S}	b Max vol fraction from M_{S}	^c TND range: monospecific assemblage (m ⁻³)	^c TND range: power law distribution (m ⁻³)
Pumice	4.97E-05	1.66E-05	8.02E-05	6.42	1.34E-05	5.14E-05	10^{13} to 10^{19}	10^{18} to 10^{19}
Northern obsidian flow	1.92E-05	6.40E-06	3.10E-05	3.47	7.23E-06	2.78E-05	10 ¹² to 10 ¹⁹	10 ¹⁸
Southern obsidian flow	9.38E-05	3.13E-05	1.51E-04	15.49	3.23E-05	1.24E-04	10^{13} to 10^{20}	10 ¹⁸ to 10 ¹⁹
Southern vesicular obsidian	1.02E-04	3.40E-05	1.65E-04	11.78	2.45E-05	9.42E-05	10^{13} to 10^{20}	10 ¹⁸ to 10 ¹⁹

^aMinimum and maximum titanomagnetite volume fractions were calculated using k values of 3 SI and 0.62 SI for Fe_3O_4 (TM0) and $Fe_{2.4}Ti_{0.60}O_4$ (TM60), respectively (values from Dunlop & Özdemir, 2015), where the TM number is the x parameter in $Fe_{3-x}Ti_xO_4$ multiplied by 100. ^bMinimum and maximum titanomagnetite volume fractions calculated using M_S values of 480 and 125 kA/m for Fe_3O_4 (TM0) and $Fe_{2.4}Ti_{0.60}O_4$ (TM60), respectively (Dunlop & Özdemir, 2015). ^cTNDs were calculated using the volume fraction derived from k_{ferro} due to the larger data set.

and have not experienced flow, compaction, or post-depositional rheomorphism. Therefore, this study focuses on the degree of anisotropy, that is, the degree to which the AMS ellipsoid deviates from a sphere, rather than absolute orientations of magnetic fabrics.

Each AMS analysis consisted of measuring the specimen in three orientations while the specimen is rotated within the applied field. The final step is a bulk susceptibility measurement. AMS measurements were used to construct a tensor that is defined by its three Eigenvectors (the principal axes) with lengths $K_1 \ge K_2 \ge K_3$, and which can be visualized as an ellipsoid (Tarling & Hrouda, 1993). The amplitudes and orientations of the maximum, intermediate, and minimum susceptibility axis, denoted K_1 , K_2 , and K_3 , respectively, are used to construct parameters that describe the fabric type and degree of anisotropy including:

Lineation parameter
$$L = K_1/K_2$$
 (6)

Foliation parameter
$$F = K_2/K_2$$
 (7)

Total anisotropy
$$P = K_1/K_3$$
 (8)

Shape parameter
$$T = \frac{(2\eta_2 - \eta_1 - \eta_3)}{(\eta_1 - \eta_3)}$$
 (9)

where η_x is the natural log of K_x and $\eta = (\eta_1 + \eta_2 + \eta_3)/3$.

T values between -1 and 0 indicate a prolate fabric, and T values between 0 and +1 indicate an oblate fabric.

3.5. X-Ray Microscopy

A whole pumice clast (0.26 cm³, 67.2% total vesicularity) was examined on a ZEISS XRadia 520 Versa at 50 kV and 4W at resolutions of 7 μ m/vx (vx = voxel, a cubic pixel), 1.8 μ m/vx and 0.7 μ m/vx, with a field of view of 14 × 14, 3.5 × 3.5, and 1.4 × 1.4 mm², and scan times of 10.5, 4.5, and 15 hr, respectively. For each scan, we used a cubic subset of 500³ voxels to perform a 3-dimensional (3D) oxide size distribution. Pixels with high gray scale values (white to bright gray) were assumed to be oxides. Only objects larger than 20 voxels were processed in each analysis to avoid noise, which sets the smallest detectable grain size at ~2.4 μ m in equivalent diameter on the 0.7 μ m/vx stack.

BRACHFELD ET AL. 6 of 15

15252027, 2024, 4, Downloaded from https://agupubs.onlinelibrary.wiley.com/doi/10.1029/2023GC011336, Wiley Online Library on [24/04/2024]. See the Terms and Conditions (https://onlinelibrary.wiley.com/terms-and-conditions) on Wiley Online Library for rules of use; OA articles are governed by the applicable Creative Commons Licenses and Conditions (https://onlinelibrary.wiley.com/terms-and-conditions) on Wiley Online Library for rules of use; OA articles are governed by the applicable Creative Commons Licenses and Conditions (https://onlinelibrary.wiley.com/terms-and-conditions) on Wiley Online Library for rules of use; OA articles are governed by the applicable Creative Commons Licenses and Conditions (https://onlinelibrary.wiley.com/terms-and-conditions) on Wiley Online Library for rules of use; OA articles are governed by the applicable Creative Commons Licenses and Conditions (https://onlinelibrary.wiley.com/terms-and-conditions) on Wiley Online Library for rules of use; OA articles are governed by the applicable Creative Commons Licenses and Conditions (https://onlinelibrary.wiley.com/terms-and-conditions) on Wiley Online Library for rules of use; OA articles are governed by the applicable Creative Commons Licenses and Conditions (https://onlinelibrary.wiley.com/terms-and-conditions) on Wiley Online Library for rules of use; OA articles are governed by the applicable Creative Commons Licenses and Conditions (https://onlinelibrary.wiley.com/terms-and-conditions) on Wiley Online Library for rules of use; OA articles are governed by the applicable Creative Commons Licenses and Conditions (https://onlinelibrary.wiley.com/terms-and-conditions) on Wiley Online Library for rules of use; OA articles are governed by the applicable Creative Commons Licenses and Conditions (https://onlinelibrary.wiley.com/terms-and-conditions) on the conditions of the conditi

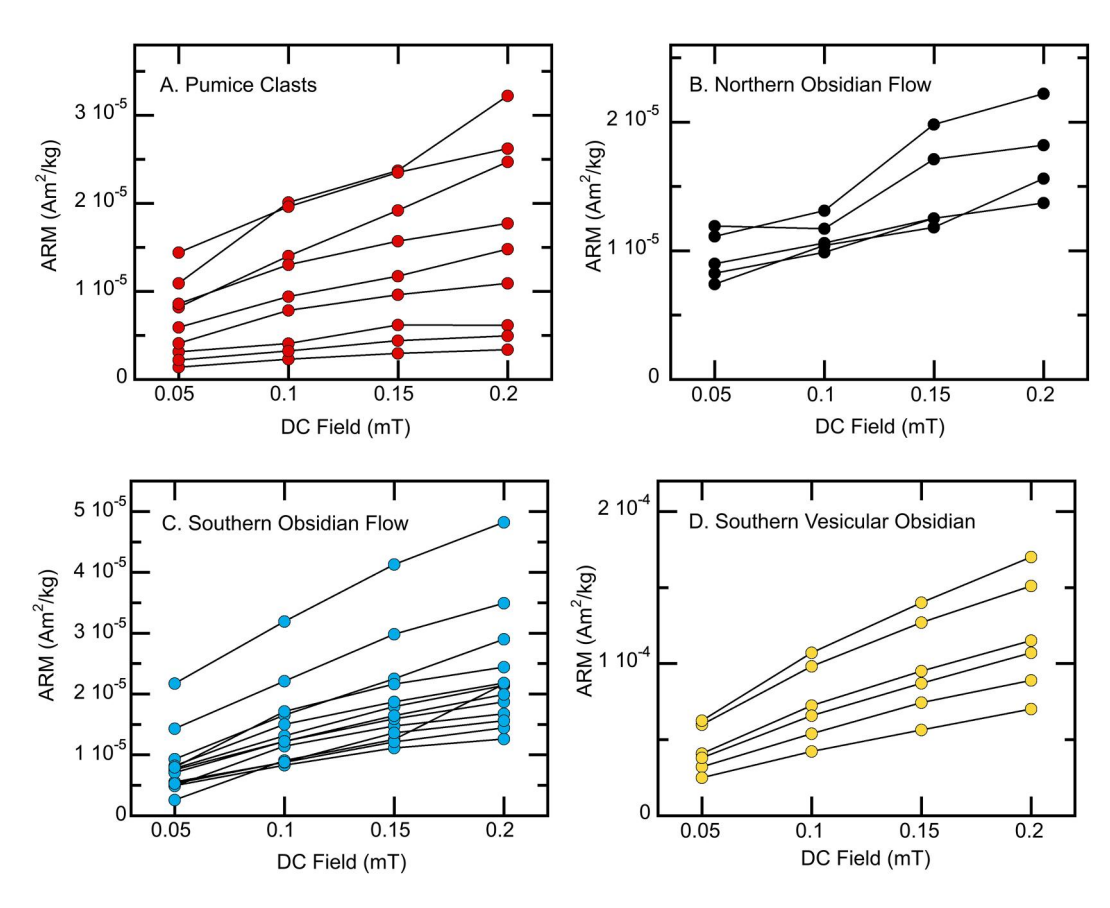


Figure 3. Anhysteretic remanent magnetization (ARM) acquisition versus direct current bias field strength ($H_{\rm DC}$) for (a) northern obsidian flow microcores, (b) southern obsidian flow pieces, (c) southern vesicular obsidian pieces, and (d) pumice cores. All eruptive and effusive products acquire an ARM whose intensity increases with $H_{\rm DC}$ amplitude, indicative of remanence-carrying stable single domain or larger particles.

4. Results

4.1. Magnetic Mineral Abundance

Glass Mountain pumice and obsidian samples have χ_{LF} values spanning 10^{-9} to 10^{-7} m³/kg (Figure 2, Table S1). The pumice sample set has the largest number of unique samples (N=198) and the greatest degree of variability. Obsidian and vesicular obsidian sample sets are smaller (N=8 to 26) and have lower variability due to specimens being cut from single blocks of obsidian. Using Equations 2–5 we calculate a maximum volume fraction of magnetic material for each sample set assuming all particles are $Fe_{2.4}Ti_{0.60}O_4$ with $k_{carrier}=0.62$ SI and $M_{S-carrier}=125$ kA/m, and a minimum volume fraction by assuming all particles are Fe_3O_4 with $k_{carrier}=3.0$ SI and $M_{S-carrier}=480$ kA/m (Dunlop & Özdemir, 2015). Volume fractions derived from k_{ferro} and M_S are very similar, generally within ~3 to 43% of each other (Table 1). The maximum-minimum ranges for the eruptive products overlap, with an absolute minimum volume fraction of 6.4×10^{-6} for the northern obsidian flow, and an absolute maximum of 1.65×10^{-4} for the southern vesicular obsidian (Figure 2, Table 1).

4.2. Magnetic Domain State

Glass Mountain pumice, obsidian, and vesicular obsidian all acquire an ARM whose intensity is dependent on H_{DC} (Figure 3, Table S2, Brachfeld et al., 2024). This indicates the presence of remanence-carrying particles, necessitating that a portion of the magnetic mineral assemblage is within the SSD or larger size range, >50–80 nm for magnetite and titanomagnetite, respectively. SP particles (<50–80 nm) are also present in pumice, as suggested by hysteresis parameters, including very low coercivities ($H_C < 3$ mT) and very low remanence ratios ($H_C < 3$) (Figure 4, Table S3, Brachfeld et al., 2024). A portion of both the pumice and obsidian sample sets plot

BRACHFELD ET AL. 7 of 15

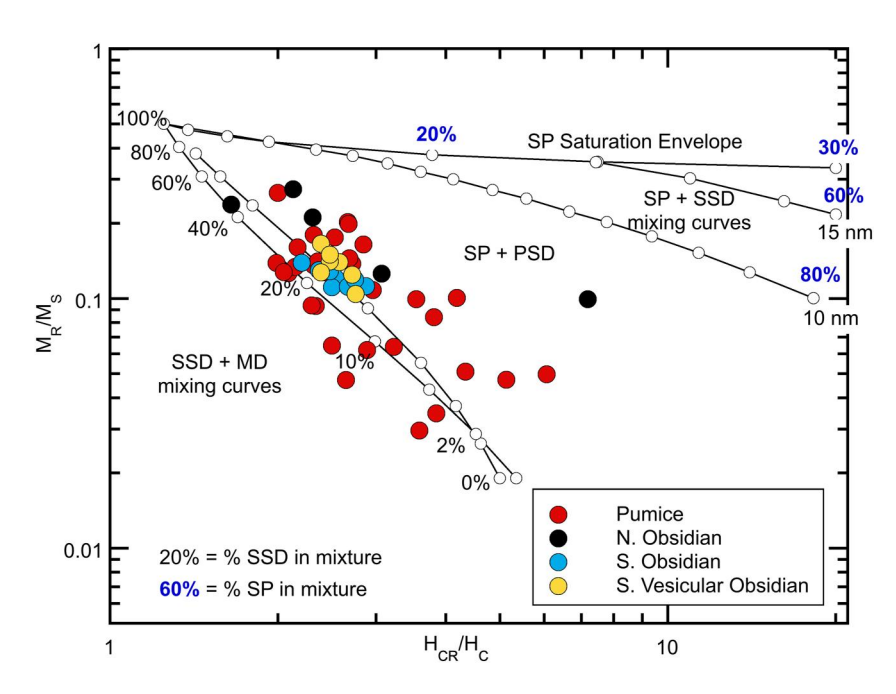


Figure 4. Day-Dunlop plot of Glass Mountain eruptive and effusive products compared with modeled two-component mixtures (Dunlop, 2002a, 2022b). Glass Mountain samples generally plot near the SSD + MD mixing lines and within the SP + PSD field.

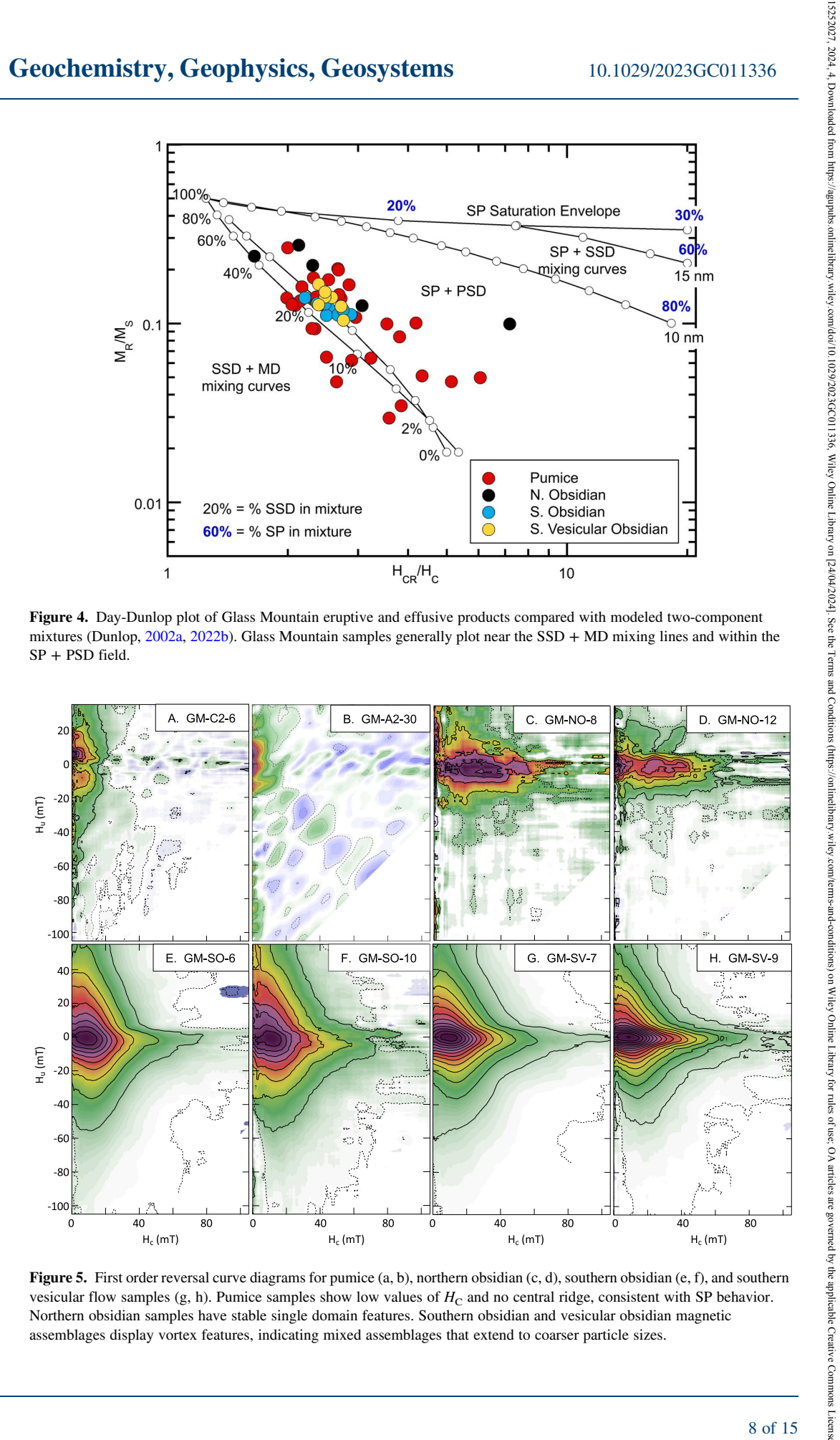


Figure 5. First order reversal curve diagrams for pumice (a, b), northern obsidian (c, d), southern obsidian (e, f), and southern vesicular flow samples (g, h). Pumice samples show low values of H_C and no central ridge, consistent with SP behavior. Northern obsidian samples have stable single domain features. Southern obsidian and vesicular obsidian magnetic assemblages display vortex features, indicating mixed assemblages that extend to coarser particle sizes.

BRACHFELD ET AL. 8 of 15

15252027, 2024, 4, Downloaded from https://agupubs.onlinelibrary.wiley.com/doi/10.1029/2023GC011356, Wiley Online Library on [24/04/2024]. See the Terms and Conditions (https://onlinelibrary.wiley.com/terms-and-conditions) on Wiley Online Library for rules of use; OA articles are governed by the applicable Creative Commons Licenses

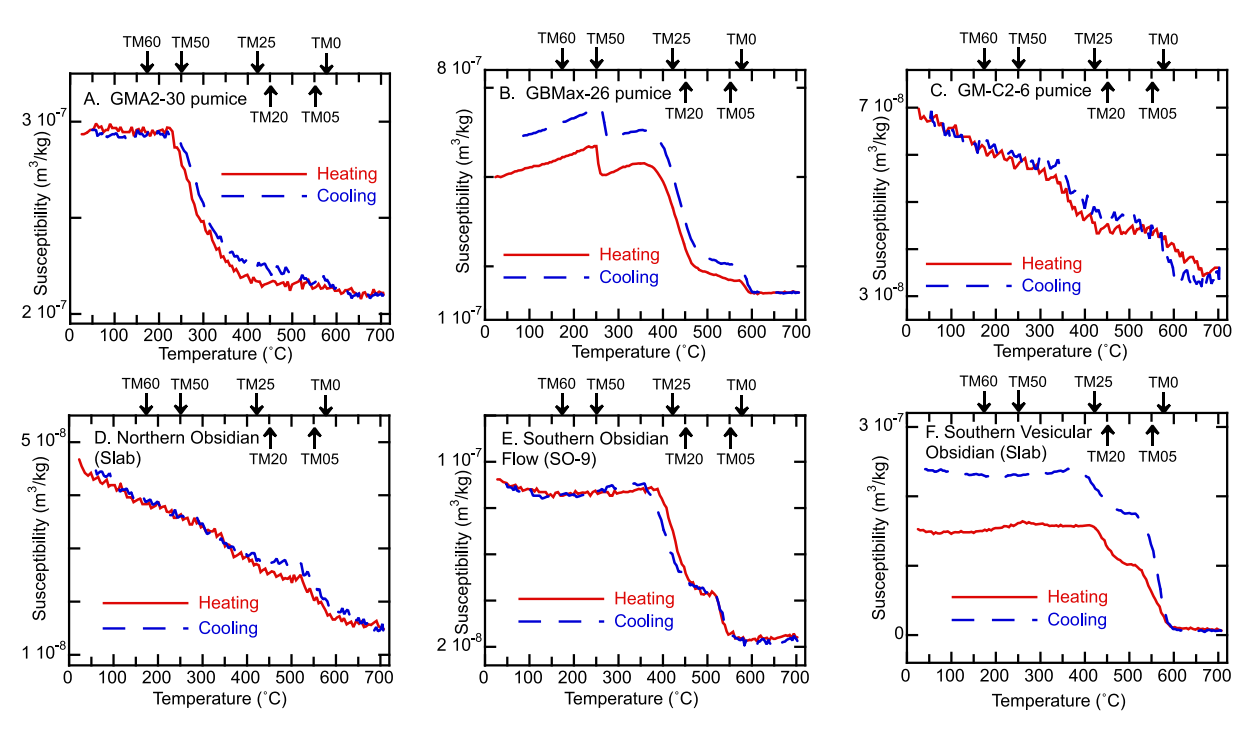


Figure 6. Thermomagnetic curves measured between 20 and 700°C during heating (red curves) and cooling (blue curves). Abrupt decreases in susceptibility indicate order-disorder transitions arising from ferrimagnetic minerals. Arrows at the top of each panel show the Curie temperatures predicted for stoichiometric titanomagnetite (expressed as TM number) using the expression of Bleil and Petersen (1982). All eruptive and effusive products (those shown here and other unpublished samples) contain one or more titanomagnetite compositions between $Fe_{2,4}Ti_{0.60}O_4$ (TM60) and Fe_3O_4 (TM0). The compositions shown here are interpreted as TM50 (AB), TM25 to TM20 (ABCEF), TM25 to TM05 (EF), and TM0 (CDF).

along the SSD + MD mixing lines on a Day-Dunlop Plot, and a portion plot within the SP + PSD mixing region (Dunlop 2002a, 2002b) (Figure 4). These mixing lines and regions are defined by experimental samples (Day et al., 1977; Parry, 1965) and modeled M-H curves with grain sizes of 10–1,000 nm for SP and SSD magnetite, respectively (Dunlop 2002a, 2002b).

FORC diagrams for pumice samples (Figures 5a and 5b) have coercivity distributions ($H_{\rm C}$) below 10–20 mT and no central ridge, consistent with SP particles. Northern obsidian samples have $H_{\rm C}$ peaks near 5 mT and 15–45 mT, reaching maximum values up to 60–80 mT, consistent with a mixture of SP and SSD particles (Figures 5c and 5d). Southern obsidian and southern vesicular obsidian FORC diagrams are very similar, with peak $H_{\rm C}$ distributions of 5–20 mT and with increased vertical spread of the contours along the $H_{\rm u}$ axis at low values of $H_{\rm C}$, indicative of a mixture of SSD, vortex and MD particles (Figures 5e–5g) (e.g., Egli, 2021).

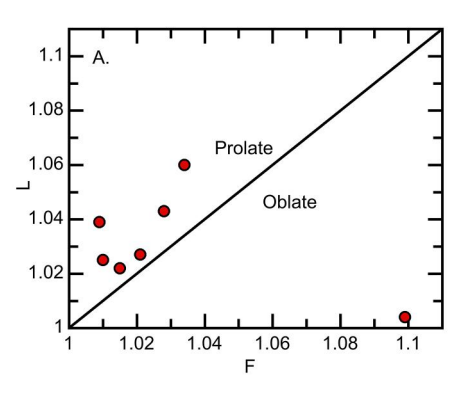
Additionally, pumice samples display $\%\chi_{fd}$ values of several % up to 26% (Table S1). Vesicular obsidian samples show low values of $\%\chi_{fd}$, and obsidian samples generally do not display frequency dependence of susceptibility (Table S1). In aggregate, pumice samples display consistent SP signatures, whereas obsidian magnetic signatures are consistent with a mixture of particle sizes spanning SP nanoparticles and extending to coarser particles in the SSD, vortex, and MD ranges.

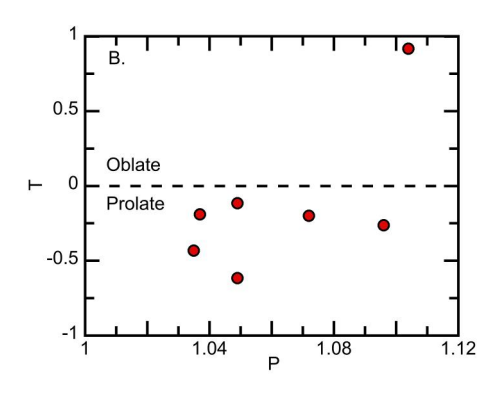
4.3. Magnetic Mineralogy

Thermomagnetic curves for all samples show one or more drops in the amplitude of χ between approximately ~200 and ~600°C, which represent Curie temperatures of titanomagnetite with variable Ti content (Figure 6). Curie temperatures above 580°C suggest slight oxidation of magnetite (Readman & O'Reilly, 1972). We also observed samples with gradual decreases in χ over broader temperature ranges (Figure 6a), which may be due to mixtures of titanomagnetite compositions and mixtures of grain sizes with different unblocking temperatures. The Curie temperatures are consistent with Fe_{2.4}Ti_{0.60}O₄ through Fe₃O₄ using the data set of Lattard et al., 2006 and the polynomial expression for T_C of Bleil and Petersen (1982).

BRACHFELD ET AL. 9 of 15

525 2027, 2024, 4, Downloaded from https://agupubs.onlinelibrary.wiley.com/doi/10.1029/2023GC011336, Wiley Online Library on [24/04/2024]. See the Terms and Conditions (https://onlinelibrary.wiley.com/terms





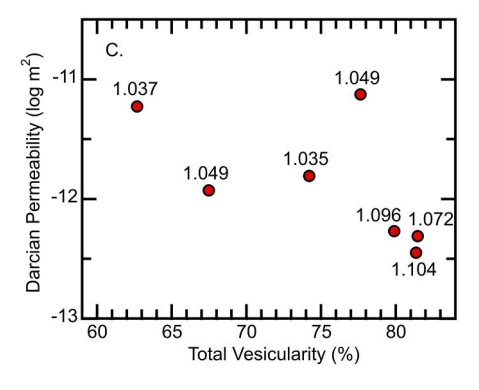


Figure 7. Anisotropy of magnetic susceptibility results from seven cylindrically cored pumice samples (Table S6). (a) All but one sample plot in the prolate region of a lineation (L) versus foliation (f) diagram. (b) Shape parameter (T) versus degree of anisotropy (P) shows that the prolate fabric is independent of the degree of anisotropy (P). (c) Darcian permeability versus total vesicularity (from McCartney et al., 2024) with associated P values. The seven pumice cores span the full range of porosity and permeability values observed in the pumice sample set. The highest P values generally coincide with the highest total vesicularity.

4.4. Anisotropy of Magnetic Susceptibility

Glass Mountain pumice cores have L values of 1.004–1.060 and F values of 1.009–1.099. Six of the seven cores have L values that are greater than F values (Figure 7, Table S4, Brachfeld et al., 2024) and negative T values, indicating prolate fabrics. Only one sample displays a high F (1.099), low L (1.004), and positive T value, indicating an oblate fabric (Figures 7a and 7b). The degree of anisotropy is high, with P values ranging from 1.035 to 1.104 (Figures 7a and 7b). Although the AMS sample set is small, the available cores span the full range of pumice vesicularity and permeability values in the full physical properties data set (McCartney et al., 2024). The highest P values coincide with the highest vesicularity (Figure 7c).

4.5. Microscopy

Inspection by optical microscopy reveals that the glass in Glass Mountain pumice is fresh and contains no evidence of devitrification such as felty groundmass texture or optical anisotropy. Published SEM examinations of pumice (Gonnermann et al., 2017; Trafton, 2021; Trafton & Giachetti, 2021) and obsidian (McCartney et al., 2024) report homogeneous glassy textures with rare microlites. In X-ray microscopy images, pixels with high gray scale values (white, bright gray) are interpreted as oxides. Crystals with equivalent grain diameters of 2.4 to \sim 53 μ m are present in pumice. Abundances determined from image analysis yield crystal number densities of 10^{13} to 10^{8} crystals m⁻³ of solid material, respectively (Figure 8a).

5. Discussion

5.1. Titanomagnetite Assemblage and Origin

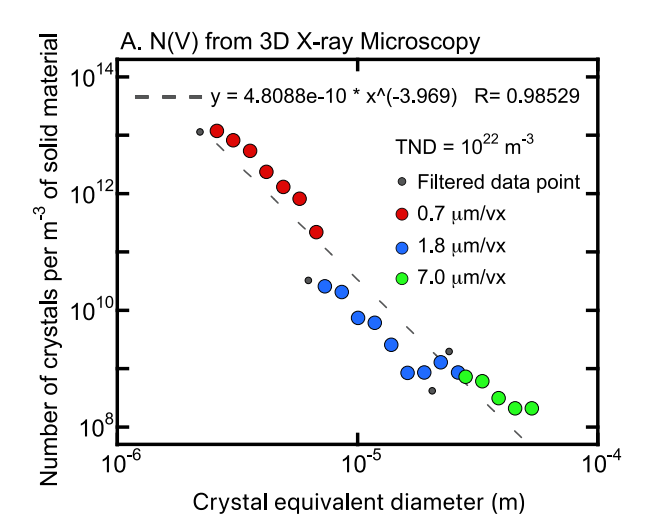
The presence of superparamagnetic iron oxides (<50–80 nm) in pumice clasts and vesicular obsidian is indicated by high values of $\%\chi_{\rm fd}$, hysteresis loops with very low H_C and very low M_R/M_S values, and FORC diagrams with very low $B_{\rm C}$ distributions. The presence of mixtures of SP, SSD (50-80 to 1,000 nm), PSD (1–10 μ m), and MD (>10 μ m) particles in pumice, obsidian, and vesicular obsidian is indicated by the acquisition of ARM, hysteresis ratios that plot along the SSD + MD mixing lines and within the SP + PSD mixing region of a Day-Dunlop plot, and FORC diagrams with central ridges, higher H_C distributions, and vertical spread of contours at low values of H_C . SEM images of Glass Mountain obsidian that capture rare microlites reveal equant oxides in the 2–20 µm size range (McCartney et al., 2024, Figure S1). These observations suggest coarsening of the existing SP population in the obsidian, likely due to the slow-moving obsidian flow remaining hot for a longer period of time than did the fragmenting pumice. However, we note that previous studies of Glass Mountain eruptive and effusive products (Giachetti et al., 2021; Grove et al., 1997; Trafton & Giachetti, 2021) have not reported devitrification textures, the mechanism proposed for the post-eruptive population of Fe-Ti oxides in the Tiva Canyon Tuff, a 100-300 m thick ash flow sheet that likely cooled over years to decades (Schlinger et al., 1988, 1991), in contrast to the rapidly cooled Glass Mountain pumice airfall deposit.

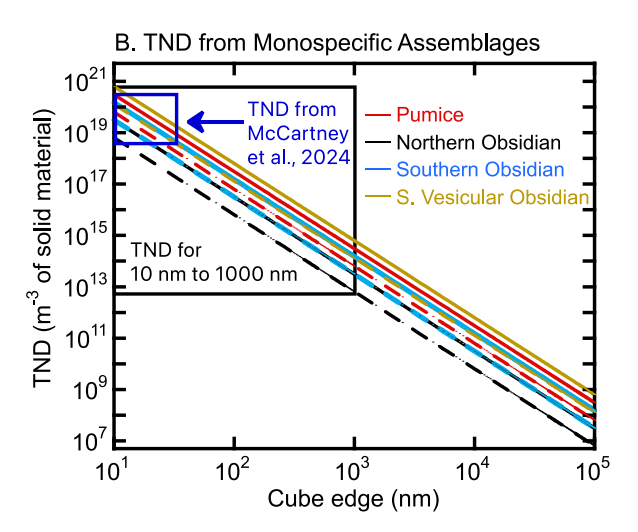
Iron oxide compositions of $Fe_{2.4}Ti_{0.60}O_4$ through Fe_3O_4 are indicated by Curie temperatures, which are generally below 580°C, with maximum observed Curie temperatures of 590–595°C. Thermomagnetic curves for both pumice and obsidian are generally reversible with minimal alteration of the sample during heating (Figures 6a, 6c–6e). One sample displays a cooling curve that is stronger than the heating curve (Figure 6b), indicative of the conversion of paramagnetic material to ferrimagnetic material during heating. However, the heating and cooling curves have the same Curie temperature features (Figures 6b and 6f). These observations argue against pervasive

BRACHFELD ET AL. 10 of 15

15252027, 2024, 4, Downloaded from https://agupubs.onlinelibrary.wiley.com/doi/10.1029/2023GC011336, Wiley Online Library on [24/04/2024]. See the Terms and Conditions (https://onlinelibrary.wiley.com/doi/10.1029/2023GC011336, Wiley Online Library on [24/04/2024]. See the Terms and Conditions (https://onlinelibrary.wiley.com/doi/10.1029/2023GC011336, Wiley Online Library on [24/04/2024]. See the Terms and Conditions (https://onlinelibrary.wiley.com/doi/10.1029/2023GC011336, Wiley Online Library.on [24/04/2024]. See the Terms and Conditions (https://onlinelibrary.wiley.com/doi/10.1029/2023GC011336, Wiley Online Library.on [24/04/2024]. See the Terms and Conditions (https://onlinelibrary.wiley.com/doi/10.1029/2023GC011336, Wiley.com/doi/10.1029/2023GC011336, Wiley.com/doi/10.1029/2023GC01136, Wiley.com/doi/10.1029/2023GC01136, Wiley.com/doi/10.1029/2023GC01136, Wiley.com/doi/10.1029/

-and-conditions) on Wiley Online Library for rules of use; OA articles are governed by the applicable Creative Commons License





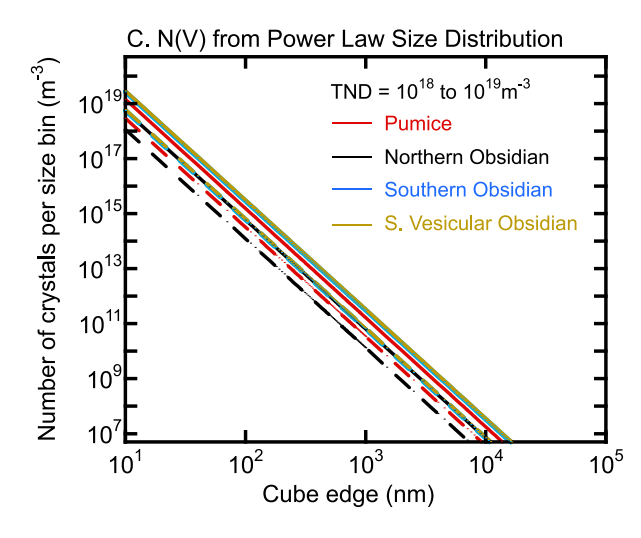


Figure 8.

maghemitization of titanomagnetite, which would be recognized by elevated Curie temperatures in the range of 620–640°C, inversion of maghemite to hematite at high temperatures, resulting in cooling curves that are weaker than the heating curves (Gehring et al., 2009; Özdemir & Banerjee, 1984), and/or the presence of new Curie features in the cooling curves as titanomaghemite inverts to a Ti-rich and a Ti-poor phase (Dunlop & Özdemir, 1997). These behaviors have been observed and attributed to the post-eruptive population of (titano)maghemite in the Tiva Canyon tuff (Rosenbaum, 1993), but are absent in Glass Mountain pumice clasts and obsidian. In aggregate, this suggests that the Glass Mountain titanomagnetite formed in the magma chamber prior to the eruption rather than in the Earth's atmosphere during or after the eruption.

Pre-eruption crystallization is also suggested by the presence of prolate fabrics in individual pumice clasts. Glass Mountain pumice clasts represent airfall deposits, and have not undergone post-emplacement transport, compaction, welding, or deformation that may occur within a pyroclastic density current and their resulting tuffs and ignimbrites. The pumice clasts are glassy materials with rare microlites due to very rapid cooling. We therefore interpret the observed fabrics to have been acquired while magnetic particles were free to rotate within a fluid, that is, prior to complete solidification of the magma. The highest degree of anisotropy coincides with the highest values of vesicularity. The prolate fabrics may have been imparted via alignment of elongated particles during the upward transport and shearing or stretching of magma following bubble nucleation, growth, and expansion at the onset of the eruption (e.g., Polacci et al., 2001; Rust et al., 2003; Shea et al., 2014). Alternately, the prolate fabric could be caused by distribution anisotropy generated by elongation of bubbles rimmed by titanomagnetite.

Bubbles rimmed by titanomagnetite, whose crystallization was facilitated by the volatiles within the bubbles, would manifest as a positive correlation between vesicularity and susceptibility. McCartney et al. (2024), tested this hypothesis and found no evidence that titanomagnetite abundance is correlated with vesicularity. However, even if this mechanism were responsible for the prolate AMS fabrics, this similarly requires that the titanomagnetite predates the passage of the liquid through the glass transition, as bubble deformation can only occur in a fluid medium.

5.2. Titanomagnetite Number Density

We use the minimum and maximum particle sizes from the Dunlop (2002a, 2002b) mixing models, 10–1,000 nm, to bracket plausible ranges of TND for each sample type. We use two methods to estimate TND. TND is first

Figure 8. (a) Number of crystals per m⁻³ of solid material derived from x-ray microscopy analysis of a Glass Mountain pumice clast. Red, blue, and green circles denote sample scans at resolutions of 0.7, 1.8, and 7.0 μm per voxel (vx = cubic pixel), respectively. Small gray circles are excluded from the power law fit to the data set (dashed gray line). (b) Maximum (solid lines) and minimum (dashed lines) titanomagnetite number densities (TND) for monospecific assemblages of cubic particles derived from the $k_{\rm ferro}$ volume fraction in Table 1. The black rectangle shows the TND range for monospecific assemblages of 10 nm (10^{20} m⁻³) through 1,000 nm (10^{12} m⁻³) particles (Table S5). The blue rectangle shows the TND results from McCartney et al. (2024), 10^{18} to 10^{20} m⁻³, for particles up to ~33 nm. (c) Number of crystals per m⁻³ of solid material derived from the power law equation in panel a. The sum of all N(V) from 10 nm to 50 μm is the TND, which ranges from 10^{18} to 10^{19} m⁻³. The two methods presented here and the low temperature method of McCartney et al. (2024) all yield consistent TND values.

BRACHFELD ET AL. 11 of 15

15252027, 2024, 4, Downloaded from https://agupubs

onlinelibrary.wiley.com/doi/10.1029/2023GC011336,

calculated by assuming a monospecific assemblage of cubic particles (i.e., all particles are the identical size, shape, and composition), and dividing the maximum and minimum titanomagnetite volume fraction by the volume of a single cube. We use the titanomagnetite volume fractions derived from k_{ferro} (N = 249) rather than M_{S} (N = 57) due to the larger susceptibility data set (Tables S1 and S3). For pumice and vesicular obsidian only, we then divide by $1 - \phi$, where ϕ is the total vesicularity expressed as a volume fraction. Average ϕ values are 0.7377 for the pumice sample set and 0.7382 for the vesicular obsidian sample set (McCartney et al., 2024). This results in TND values per m⁻³ of solid material (the DRE), that is, on a vesicle-free basis. This form of the TND represents the number density prior to vesiculation within the magma. For monospecific assemblages of 1,000–10 nm cubes, this translates to TNDs of 10^{12} to 10^{20} particles per m³, respectively (Figure 8b and Table 1, Table S5).

As monospecific assemblages do not occur in nature, we present a second method of estimating TND that extrapolates the trend determined from the analysis of X-ray microscopy microlite observations in Glass Mountain pumice. Summing the particles in all bins in Figure 8a yields a microlite number density of $\sim 2.95 \times 10^{13}$ m⁻³ of solid material. As a sensitivity test, we filtered out the smallest size bin in each of the three resolution scans. For overlapping size bins, we retained the higher resolution data set and excluded the lower resolution data set. Summing the particles in the filtered data set yields a microlite number density of 1.90×10^{13} m⁻³ of solid material. The variation is less than a factor of two due to the finest size bins controlling the number density. We fit a power law equation $y = Ax^k$ to the filtered data set and extrapolated the size distribution to 10 nm, which results in an oxide number density of $\sim 10^{22}$ m⁻³ for the analyzed pumice clast. We then use the power law equation to generate a grain size and volume distribution between 10 nm and 50 μ m. Using the k_{ferro} -derived average volume fraction for eruptive and effusive products (Table 1), we allocate the volume fraction contained within each grain size bin. We then calculate the number of cubic particles necessary to generate each volume fraction at each grain size. The sum of all particles between 10 nm and 50 μ m is the TND. This method yields TNDs of 10^{18} to 10^{19} m⁻³ of solid material for Glass Mountain pumice, obsidian, and vesicular obsidian (Figure 8c, Table S6).

A low-temperature TND determination for pumice of 10^{18} to 10^{20} m⁻³ is presented in McCartney et al. (2024), in which the distribution of magnetic particle blocking volumes is determined from the thermal unblocking of a TRM imparted below room temperature at 5 K (Wörm & Jackson, 1999). This method exploits the transition in nanoparticle SP behavior at room temperature to SSD behavior below room temperature. This method makes no a priori assumptions about the particle sizes present or the size distribution. The two TND calculations presented here are comparable to the results of McCartney et al. (2024). All three methods support the hypothesis that submicron titanomagnetite crystals are abundant in these aphyric and silicic rocks and potential sites for bubble nucleation during magma ascent.

6. Conclusions

We use magnetic methods to document the presence of titanomagnetite nanolites and ultra-nanolites in aphyric rhyolitic rocks. Magnetic methods enable the characterization of titanomagnetite composition, domain state, and number densities in materials with extremely low volume fractions of magnetic material, 6.4×10^{-6} to 1.65×10^{-4} for Glass Mountain effusive and eruptive products, respectively, and in samples where conventional petrographic characterization is extremely challenging. ARM, hysteresis properties, and frequency dependence of magnetic susceptibility indicate a range of domain states are present in pumice, obsidian, and vesicular obsidian, spanning superparamagnetic nanoparticles through multidomain microlites. Prolate magnetic fabrics were observed in pumice clasts, with the highest degree of anisotropy coinciding with the highest vesicularity. This may represent a flow fabric acquired at the onset of the eruption as bubble nucleation drove magma ascent. TND determinations for monospecific grain size assemblages range from 10^{12} to 10^{20} m⁻³ for cubic particles with edge lengths of 1,000–10 nm, respectively, and 10^{18} to 10^{19} m⁻³ for a power law grain size distribution spanning 10 nm to 50 μ m, in agreement with the results of McCartney et al. (2024). This demonstrates that plausible TND estimates can be obtained from rock magnetic measurements made at room temperature. In aggregate, our results support the hypothesis that titanomagnetite is an abundant and early forming phase in rhyolitic magma from Glass Mountain, with the potential to influence eruption dynamics.

BRACHFELD ET AL. 12 of 15

and-conditions) on Wiley Online Library for rules of use; OA articles are governed by the applicable Creative Commons Licens

Data Availability Statement

Magnetic data in this study is contained in the supplemental tables of this publication, and archived with the Magnetics Information Consortium (MagIC) at https://doi.org/10.7288/V4/MAGIC/20020.

Acknowledgments

This work was supported by National Science Foundation Grant 1839313 to Montclair State University and 1839230 to the University of Hawaii, NSF Grant 1342000 to Montclair State University cofunded the MFK-2A Kappabridge. We thank Melissa Hansen for assistance with magnetic measurements at Montclair State University, and express our sincere gratitude to NSF program director Dr. Jennifer Wade for her support during this project. We thank two anonymous reviewers for their constructive comments that improved this manuscript, and Joshua Feinberg and Sophie Hanson for administrative handling of this manuscript

References

- Argyle, K. S., & Dunlop, D. J. (1990). Low-temperature and high-temperature hysteresis of small multidomain magnetites (215–540 nm). *Journal of Geophysical Research*, 95(B5), 7069–7083. https://doi.org/10.1029/JB095iB05p07069
- Aubin, W. L., Gardner, J. E., Watkins, J. M., & Lloyd, M. H. (2023). Construction of obsidian during explosive-effusive eruptions: Insights from microlite crystals in obsidian pyroclasts. Frontiers in Earth Science, 11, 1183923. https://doi.org/10.3389/feart.2023.1183923
- Bleil, U., & Petersen, N. (1982). Magnetic properties of natural minerals. In G. Angenheister (Ed.), Numerical data and functional relationships in science and technology, group V: Geophysics and space research (pp. 308–365). Springer.
- Brachfeld, S., McCartney, K. N., Hammer, J. E., Shea, T., & Giachetti, T. (2024). Evaluating the role of titanomagnetite in bubble nucleation:
 Rock magnetic detection and characterization of nanolites and ultra-nanolites in rhyolite pumice and obsidian from Glass Mountain, California
 [Dataset]. Magnetics Information Consortium (MagIC). https://doi.org/10.7288/V4/MAGIC/20020
- Cáceres, F., Scheu, B., Hess, K.-U., Cimarelli, C., Vasseur, J., Kaliwoda, M., & Dingwell, D. B. (2021). From melt to crystals: The effects of cooling on Fe–Ti oxide nanolites crystallisation and melt polymerisation at oxidising conditions. *Chemical Geology*, 563, 120057. https://doi.org/10.1016/j.chemgeo.2021.120057
- Cáceres, F., Wadsworth, F. B., Scheu, B., Colombier, M., Madonna, C., Cimarelli, C., et al. (2020). Can nanolites enhance eruption explosivity? Geology, 48(10), 997–1001. https://doi.org/10.1130/G47317.1
- Day, R., Fuller, M., & Schmidt, V. (1977). Hysteresis properties of titanomagnetites: Grain size and compositional dependence. *Physics of the Earth and Planetary Interiors*, 13(4), 260–267. https://doi.org/10.1016/0031-9201(77)90108-X
- Dearing, J. A., Dann, R. J. L., Hay, K., Lees, J. A., Loveland, P. J., Maher, B. A., & O'Grady, K. (1996). Frequency-dependent susceptibility measurements of environmental materials. *Geophysical Journal International*, 124(1), 228–240. https://doi.org/10.1111/j.1365-246X.1996.
- Di Genova, D., Brooker, R. A., Mader, H. M., Drewitt, J. W. E., Longo, A., Deubener, J., et al. (2020). In situ observation of nanolite growth in volcanic melt: A driving force for explosive eruptions. *Science Advances*, 6(39), eabb0413. https://doi.org/10.1126/sciadv.abb0413
- Di Genova, D., Kolzenburg, S., Wiesmaier, S., Dallanave, E., Neuville, D. R., Hess, K.-U., & Dingwell, D. B. (2017). A compositional tipping point governing the mobilization and eruption style of rhyolitic magma. *Nature*, 552(7684), 235–238. https://doi.org/10.1038/nature24488
- Dunlop, D. J. (1986). Hysteresis properties of magnetite and their dependence on particle size: A test of PSD remanence models. *Journal of Geophysical Research*, 91(B9), 9569–9584. https://doi.org/10.1029/JB091iB09p09569
- Dunlop, D. J. (2002a). Theory and application of the Day plot (Mrs/Ms versus Hcr/Hc) 1. Theoretical curves and tests using titanomagnetite data. Journal of Geophysical Research, 107(B3), 2056. https://doi.org/10.1029/2001JB000486
- Dunlop, D. J. (2002b). Theory and application of the Day plot (Mrs/Ms versus Hcr/Hc) 2. Application to data for rocks, sediments, and soils. Journal of Geophysical Research, 107(B3), 2057. https://doi.org/10.1029/2001JB000487
- Dunlop, D. J., & Argyle, K. S. (1997). Thermoremanence, anhysteretic remanence, and susceptibility of submicron magnetites: Non-linear field dependence and variation with grain size. *Journal of Geophysical Research*, 102(B9), 20199–20210. https://doi.org/10.1029/97JB00957
- Dunlop, D. J., & Özdemir, Ö. (1997). Rock magnetism: Fundamentals and frontiers. Cambridge University Press. https://doi.org/10.1017/
- Dunlop, D. J., & Özdemir, Ö. (2015). 5.08 magnetizations in rocks and minerals. In G. Schubert & M. Kono (Eds.), *Treatise on Geophysics*, volume 5: Geomagnetism (2nd ed., p. 530). Elsevier Earth Systems and Environmental Sciences. https://doi.org/10.1016/B978-0-444-53802-4.
- Egli, R. (2013). VARIFORC: An optimized protocol for calculating non-regular first-order reversal curve (FORC) diagrams. *Global and Planetary Change*, 110(Part C), 302–320. https://doi.org/10.1016/j.gloplacha.2013.08.003
- Egli, R. (2021). Magnetic characterization of geologic materials with first- order reversal-curves. In V. Franco & B. Dodrill (Eds.), Magnetic measurement techniques for materials characterization (p. 815). Springer International Publishing Group. https://doi.org/10.1007/978-3-030-70443-8-17
- Ellwood, B. B. (1982). Estimates of flow direction for calc-alkaline welded tufts and paleomagnetic data reliability from anisotropy of magnetic susceptibility measurements: Central San Juan Mountains, southwest Colorado. Earth and Planetary Science Letters, 59(2), 303–314. https://doi.org/10.1016/0012-821X(82)90133-9
- Gardner, J. E., & Denis, M.-H. (2004). Heterogeneous bubble nucleation on Fe-Ti oxide crystals in high-silica rhyolitic melts. *Geochimica et Cosmochimica Acta*, 68(7), 3587–3597. https://doi.org/10.1016/j.gca.2004.02.021
- Gehring, A. U., Fischer, H., Louvel, M., Kunze, K., & Weidler, P. G. (2009). High temperature stability of natural maghemite: A magnetic and spectroscopic study. Geophysical Journal International, 179(3), 1361–1371. https://doi.org/10.1111/j.1365-246X.2009.04348.x
- Giachetti, T., Burgisser, A., Arbaret, L., Druitt, T. H., & Kelfoun, K. (2011). Quantitative textural analysis of Vulcanian pyroclasts (Montserrat) using multi-scale X-ray computed microtomography: Comparison with results from 2D image analysis. *Bulletin of Volcanology*, 73(9), 1295–1309. https://doi.org/10.1007/s00445-011-0472-1
- Giachetti, T., Druitt, T. H., Burgisser, A., Arbaret, L., & Galven, C. (2010). Bubble nucleation and growth during the 1997 Vulcanian explosions of Soufrière Hills volcano, Montserrat. *Journal of Volcanology and Geothermal Research*, 193(3–4), 215–231. https://doi.org/10.1016/j.jvolgeores.2010.04.001
- Giachetti, T., Gonnermann, H. M., Gardner, J. E., Shea, T., & Gouldstone, A. (2015). Discriminating secondary from magmatic water in rhyolitic matrix-glass of volcanic pyroclasts using thermogravimetric analysis. *Geochimica et Cosmochimica Acta*, 148, 457–476. https://doi.org/10. 1016/j.gca.2014.10.017
- Giachetti, T., Trafton, K. R., Wiejaczka, J., Gardner, J. E., Watkins, J. M., Shea, T., & Wright, H. M. N. (2021). The products of primary magma fragmentation finally revealed by pumice agglomerates. *Geology*, 49(11), 1307–1311. https://doi.org/10.1130/G48902.1
- Gonnermann, H. M., Giachetti, T., Fliedner, C., Nguyen, C. T., Houghton, B. F., Crozier, J. A., & Carey, R. J. (2017). Permeability during magma expansion and compaction. *Journal of Geophysical Research: Solid Earth*, 122(12), 9825–9848. https://doi.org/10.1002/2017JB014783
- Grove, T. L., Donnelly-Nolan, J. M., & Housh, T. (1997). Magmatic processes that generated the rhyolite of Glass Mountain, Medicine Lake Volcano, N. California. *Contributions to Mineralogy and Petrology*, 127(3), 205–223. https://doi.org/10.1007/S004100050276

BRACHFELD ET AL. 13 of 15

- Hajimirza, S., Gonnermann, H. M., & Gardner, J. E. (2021). Reconciling bubble nucleation in explosive eruptions with geospeedometers. *Nature Communications*, 12(1), 283. https://doi.org/10.1038/s41467-020-20541-1
- Harrison, R. J., & Feinberg, J. M. (2008). FORCinel: An improved algorithm for calculating first-order reversal curve distributions using locally weighted regression smoothing. Geochemistry, Geophysics, Geosystems, 9(5), Q05016. https://doi.org/10.1029/2008GC001987
- Harrison, R. J., Muraszko, J., Heslop, D., Lascu, I., Muxworthy, A. R., & Roberts, A. P. (2018). An improved algorithm for unmixing first-order reversal curve diagrams using principal component analysis. *Geochemistry, Geophysics, Geosystems*, 19(5), 1595–1610. https://doi.org/10. 1029/2018GC007511
- Hartstra, R. L. (1982). Grain-size dependence of initial susceptibility and saturation Magnetization-related parameters of four natural magnetites in the PSD-MD range. *Geophysical Journal of the Royal Astronomical Society*, 71(2), 477–495. https://doi.org/10.1111/j.1365-246X.1982.
- Heiken, G. (1978). Plinian-type eruptions in the Medicine Lake Highland, California, and the nature of the underlying magma. *Journal of Volcanology and Geothermal Research*, 4(3-4), 375-402. https://doi.org/10.1016/0377-0273(78)90023-9
- Knafelc, J., Bryan, S. E., Jones, M. W. M., Gust, D., Mallmann, G., Cathey, H. E., et al. (2022). Havre 2012 pink pumice is evidence of a short-lived, deep-sea, magnetite nanolite-driven explosive eruption. *Nature Communications*, 3(1), 19. https://doi.org/10.1038/s43247-022-00355-3
- Lattard, D., Engelmann, R., Kontny, A., & Sauerzapf, U. (2006). Curie temperatures of synthetic titanomagnetites in the Fe-Ti-O system: Effects of composition, crystal chemistry, and thermomagnetic methods. *Journal of Geophysical Research*, 111(B12S28), 1–18. https://doi.org/10.1029/2006/B004591
- Maher, B. A. (1988). Magnetic properties of some synthetic sub-micron magnetite's. *Geophysical Journal International*, 94(1), 83–96. https://doi.org/10.1111/j.1365-246X.1988.tb03429.x
- McCartney, K. N., Hammer, J. E., Shea, T., Brachfeld, S., & Giachetti, T. (2024). Investigating the role of nanoscale titanomagnetite in bubble nucleation via novel applications of magnetic analyses. *Geochemistry, Geophysics, Geosystems*, e2023GC011338. https://doi.org/10.1029/2023GC011338
- Mujin, M., & Nakamura, M. (2014). A nanolite record of eruption style transition. *Geology*, 42(7), 611–614. https://doi.org/10.1130/G35553.1 Mujin, M., Nakamura, M., & Miyake, A. (2017). Eruption style and crystal size distributions: Crystallization of groundmass nanolites in the 2011 Shinmoedake eruption. *American Mineralogist*, 102(12), 2367–2380. https://doi.org/10.2138/am-2017-6052CCBYNCND
- Ort, M. H., Newkirk, T. T., Vilas, J. F., & Vazquez, J. A. (2015). Towards the definition of AMS facies in the deposits of pyroclastic density currents. In M. H. Ort, M. Porreca, & J. W. Geissman (Eds.), *The use of palaeomagnetism and rock magnetism to understand volcanic processes* (Vol. 396, pp. 205–226). Geological Society, London, Special Publications. https://doi.org/10.1144/sp396.8
- Özdemir, Ö., & Banerjee, S. K. (1982). A preliminary magnetic study of soil samples from west-central Minnesota. *Earth and Planetary Science Letters*, 59(2), 393–403. https://doi.org/10.1016/0012-821X(82)90141-8
- Özdemir, Ö., & Banerjee, S. K. (1984). High temperature stability of maghemite (γ-Fe₂O₃). Geophysical Research Letters, 11(3), 161–164. https://doi.org/10.1029/GL011i003p00161
- Palmer, H. C., MacDonald, W. D., Gromme, C. S., & Ellwood, B. B. (1996). Magnetic properties and emplacement of the Bishop tuff, California. Bulletin of Volcanology, 58(2–3), 101–116. https://doi.org/10.1007/s004450050129
- Parry, L. G. (1965). Magnetic properties of dispersed magnetite powders. *Philosophical Magazine*, 11(110), 303–312. https://doi.org/10.1080/14786436508221858
- Pistone, M., Forma, E., Whittington, A. G., Thomas Herbst, T., & Cottrell, E. (2022). Direct nanoscale observations of degassing-induced crystallisation in felsic magmas. *Contributions to Mineralogy and Petrology*, 177(3), 38. https://doi.org/10.1007/s00410-022-01900-1
- Polacci, M., Papale, P., & Rosi, M. (2001). Textural heterogeneities in pumices from the climactic eruption of Mount Pinatubo, 15 June 1991, and implications for magma ascent dynamics. *Bulletin of Volcanology*, 63(2–3), 83–97. https://doi.org/10.1007/s004450000123
- Readman, P. W., & O'Reilly, W. O. (1972). Magnetic properties of oxidized (cation-deficient) titanomagnetites (Fe, Ti, [])₃O₄. *Journal of Geomagnetism and Geoelectricity*, 24(1), 69–90. https://doi.org/10.5636/jgg.24.69
- Roberts, A. P., Almeida, T. P., Church, N. S., Harrison, R. J., Heslop, D., Li, Y., et al. (2017). Resolving the origin of pseudo-single domain magnetic behavior. *Journal of Geophysical Research: Solid Earth*, 122(12), 9534–9558. https://doi.org/10.1002/2017JB014860
- Rosenbaum, J. G. (1993). Magnetic grain size variations through an ash flow sheet: Influence on magnetic properties and implications for cooling history. *Journal of Geophysical Research*, 98(B7), 11715–11727. https://doi.org/10.1029/93JB00355
- Rust, A. C., Manga, M., & Cashman, K. V. (2003). Determining flow type, shear rate and shear stress in magmas from bubble shapes and orientations. *Journal of Volcanology and Geothermal Research*, 122(1–2), 111–132, https://doi.org/10.1016/S0377-0273(02)00487-0
- Schlinger, C. M., Rosenbaum, J. G., & Veblen, D. R. (1988). Fe-oxide microcrystals in welded tuff from southern Nevada: Origin of remanence carriers by precipitation in volcanic glass. *Geology*, 16(6), 556–559. https://doi.org/10.1130/0091-7613(1988)016<0556:FOMIWT>2.3.CO;2
- Schlinger, C. M., Veblen, D. R., & Rosenbaum, J. G. (1991). Magnetism and magnetic mineralogy of ashflow tuffs from Yucca Mountain, Nevada. *Journal of Geophysical Research*, 96(B4), 6035–6052. https://doi.org/10.1029/90JB02653
- Sharp, T. G., Stevenson, R. J., & Dingwell, D. B. (1996). Microlites and "nanolites" in rhyolitic glass: Microstructural and chemical characterization. Bulletin of Volcanology, 57(8), 631–640. https://doi.org/10.1007/s004450050116
- Shea, T. (2017). Bubble nucleation in magmas: A dominantly heterogeneous process? *Journal of Volcanology and Geothermal Research*, 343, 155–170. https://doi.org/10.1016/j.jvolgeores.2017.06.025
- Shea, T., Hellebrand, E., Gurioli, L., & Tuffen, H. (2014). Conduit-to localized-scale degassing during Plinian eruptions: Insights from major element and volatile (Cl and H₂O) analyses within Vesuvius ad 79 pumice. *Journal of Petrology*, 55(2), 315–344. https://doi.org/10.1093/petrology/egt069
- Sugiura, N. (1979). ARM, TRM and magnetic interactions: Concentration dependence. Earth and Planetary Science Letters, 42(3), 451–455. https://doi.org/10.1016/0012-821X(79)90054-2
- Tarling, D. H., & Hrouda, F. (1993). The magnetic anisotropy of rocks. Chapman & Hall. https://doi.org/10.1002/gj.3350300111
- Tauxe, L., Bertram, H. N., & Seberino, C. (2002). Physical interpretation of hysteresis loops: Micromagnetic modeling of fine particle magnetite. Geochemistry, Geophysics, Geosystems, 3(10), 1–22. https://doi.org/10.1029/2001GC000241
- Trafton, K. R. (2021). Pyroclasts: A window into the volcanic conduit (doctoral dissertation). University of Oregon.
- Trafton, K. R., & Giachetti, T. (2021). The morphology and texture of Plinian pyroclasts reflect their lateral sourcing in the conduit. Earth and Planetary Science Letters, 562, 116844. https://doi.org/10.1016/j.epsl.2021.116844
- Vigliotti, L., Bilardello, D., Winkler, A., & Del Carlos, P. (2022). Rock magnetic fingerprint of Mt Etna volcanic ash. Geophysical Journal International, 231(2), 749–769. https://doi.org/10.1093/gji/ggac213
- Williams, W., & Dunlop, D. J. (1995). Simulation of magnetic hysteresis in pseudo-single-domain grains of magnetite. *Journal of Geophysical Research*, 100(B3), 3859–3871. https://doi.org/10.1029/94JB02878

BRACHFELD ET AL. 14 of 15

Wolff, J. A., Ellwood, B. B., & Sachs, S. D. (1989). Anisotropy of magnetic susceptibility in welded tufts: Application to a welded-tuff dyke in the tertiary trans-pecos Texas volcanic province, USA. *Bulletin of Volcanology*, 51(4), 299–310. https://doi.org/10.1007/BF01073518

Wörm, H.-U., & Jackson, M. (1999). The superparamagnetism of Yucca mountain tuff. *Journal of Geophysical Research*, 104(B11), 25415—25425. https://doi.org/10.1029/1999JB900285

Yoshida, K., Miyake, A., Okumura, S. H., Ishibashi, H., Okumura, S., Okamoto, A., et al. (2023). Oxidation-induced nanolite crystallization triggered the 2021 eruption of Fukutoku-Oka-no-Ba, Japan. *Nature Scientific Reports*, 13(1), 7117. https://doi.org/10.1038/s41598-023-34301-w

BRACHFELD ET AL. 15 of 15